Scene estimation from speckled synthetic aperture radar imagery: Markov-random-field approach

Ousseini Lankoande, Majeed M. Hayat, and Balu Santhanam

Department of Electrical and Computer Engineering, MSC01 1100, 1 University of New Mexico, Albuquerque, New Mexico 87131-0001

Received June 1, 2005; revised November 21, 2005; accepted December 18, 2005; posted January 11, 2006 (Doc. ID 62507)

A novel Markov-random-field model for speckled synthetic aperture radar (SAR) imagery is derived according to the physical, spatial statistical properties of speckle noise in coherent imaging. A convex Gibbs energy function for speckled images is derived and utilized to perform speckle-compensating image estimation. The image estimation is formed by computing the conditional expectation of the noisy image at each pixel given its neighbors, which is further expressed in terms of the derived Gibbs energy function. The efficacy of the proposed technique, in terms of reducing speckle noise while preserving spatial resolution, is studied by using both real and simulated SAR imagery. Using a number of commonly used metrics, the performance of the proposed technique is shown to surpass that of existing speckle-noise-filtering methods such as the Gamma MAP, the modified Lee, and the enhanced Frost. © 2006 Optical Society of America

OCIS codes: 100.0100, 110.0110, 030.0030, 280.0280.

1. INTRODUCTION

A key advantage of synthetic aperture radar (SAR) over passive systems for imaging Earth's surface is that it is independent of any source that is external to the system (e.g., sunlight). A SAR system emits its own radiation, which is typically in the microwave to centimeter-wave range of the electromagnetic spectrum. Additionally, their relatively long wavelengths, compared with those of passive and active optical sensors, make SAR systems capable of imaging the Earth's surface regardless of weather conditions such as dust, cloud cover, and fog.[1] Moreover, the usual limitations imposed on the size of a physical antenna are lifted through the use of a synthetic aperture, which synthesizes a large antenna by coherently processing the signals received by a moving, smaller antenna.[1] This has allowed SAR systems to achieve remarkably good resolutions. Indeed, although the resolution depends on the observed target, impressive 4-in. resolution has been attained with an airborne system called "Lynx," designed by Sandia National Laboratories (SNL) and produced by General Atomic.[2]

Unfortunately, the efficiency of aerial data collection and visualization with SAR systems is often impeded by their high susceptibility to speckle noise. A SAR system measures both the amplitude and phase of the signals echoed from the Earth's surface. However, due to the microscopic surface roughness of the reflecting objects on the ground, the amplitudes of the echoed signals reflected from the locality of each targeted spot have random phases. The amplitudes of these signals interfere coherently at the antenna, which ultimately gives rise to the signal-dependent and grainy speckle noise formed in the SAR imagery.[1,3,4]

A large variety of speckle-reduction techniques have been developed and proposed in the literature. Representatives of these techniques include the Lee filter and its derivatives,[5,6] the geometric filter,[7] the Kuan filter,[8] the Frost filter and its derivatives,[6,9] the Gamma MAP filter,[6] the wavelet approach,[10,11] and the approaches based on Markov random fields (MRFs).[12,13] A common assumption in these approaches is that speckle noise is multiplicative to the image intensity. [14] This assumption can be useful in simplifying the complex nature of speckled imagery and partially capturing the signal-dependent nature of speckle noise. In actuality, however, speckle noise is neither multiplicative nor additive to the image intensity.[15–17] Furthermore, speckled imagery does possess special spatial-correlation characteristics that have been established in the statistical-optics literature[18,19] but have not been exploited, to the best of our knowledge, in reducing speckle noise.

In this paper, we introduce a new framework for modeling speckled SAR imagery that is based on MRFs in conjunction with the physical statistical characteristics of speckle.[18,19] The capability of MRFs to model spatially correlated and signal-dependent phenomena makes them an excellent choice for modeling speckled images without the need to adopt a multiplicative-noise assumption. In addition, they can lend themselves to many statistical image-processing strategies that are not predicated on any multiplicative- or additive-noise assumptions. In particular, we consider the speckled image as a realization of the proposed MRF model with high energy, which is a consequence of the high variability of the pixel intensities due to the presence of speckle noise. We have embedded Goodman's[18] joint conditional probability density function (cpdf) of the speckled intensity of any two points into the MRF framework, which makes the resulting MRF consistent with the physical attributes of speckled imagery. We then develop and test a speckle-compensating image esti-

1084-7529/06/061269-13/$15.00

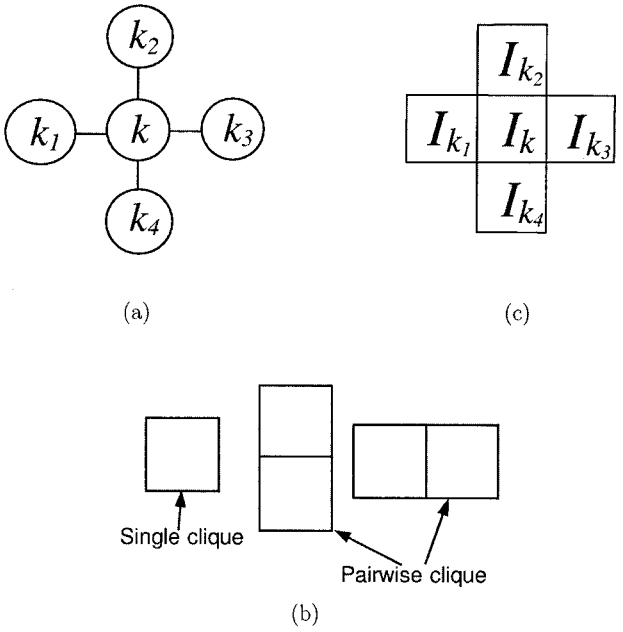

Fig. 1. (a) Segment of the graph representing the first-order MRF. (b) Illustration of two types of cliques. (c) Neighborhood of the pixel k according to the first-order MRF. I_{k_i} corresponds to the k_ith pixel value.

mation algorithm, which is a model-based conditional estimator of the speckle-free SAR image. Thanks to the MRF framework, this estimator is conveniently expressed in terms of the conditional expectation of a pixel given its neighbors. Indeed, this image estimator reduces the energy of the speckled image, which, in turn, reduces the speckle noise. The proposed speckle-reduction approach is applied to both simulated and real SAR imagery, and the results are compared with those from existing speckle-reduction techniques.

2. MODEL

The proposed first-order MRF consists of an undirected graph $G=(V,E)$ that has undirected edges drawn as lines. The set of vertices of a segment of the graph, centered at the kth pixel graph, is given by $V=\{k,k_1,k_2,k_3,k_4\}$, as shown in Fig. 1(a), and E is the set of edges. From the graph G, two types of cliques are extracted: the single clique and the pairwise clique, as depicted in Fig. 1(b). A single clique C_1 is simply any individual pixel in the image; a pairwise clique C_2 is a set of any two vertically adjacent or horizontally adjacent pixels. An example of the neighborhood of a pixel k is shown in Fig. 1(c).

A. Description of the Markov-Random-Field Conditional Probability Density Function

Goodman[18] has derived the cpdf of the intensity I_{k_j} at point k_j given the value of the intensity I_{k_i} at point k_i. In this work, we have replaced the spatially constant mean $\langle I\rangle$, used by Goodman,[18] with $\mathcal{O}_{k_j}$, which is defined as the spatially inhomogeneous true intensity image at point k_j. If we denote the realization of the random variable I_{k_j} at point k_j by i_{k_j}, then the cpdf is given by

$$p_{I_{k_j}|I_{k_i}}(i_{k_j}|i_{k_i}) = \frac{\exp\left\{-\dfrac{|\mu(r_{k_ik_j})|^2 i_{k_i}+i_{k_j}}{[I-|\mu(r_{k_ik_j})|^2]\mathcal{O}_{k_j}}\right\}}{[1-|\mu(r_{k_ik_j})|^2]\mathcal{O}_{k_j}} \mathcal{I}_0\left(\frac{2\sqrt{i_{k_i}i_{k_j}}|\mu(r_{k_ik_j})|}{[1-|\mu(r_{k_ik_j})|^2]\mathcal{O}_{k_j}}\right), \tag{1}$$

where $\mathcal{I}_0(\cdot)$ is a modified Bessel function of the first kind and zero order, and $|\mu(r_{k_ik_j})|$ and $r_{k_ik_j}$ are, respectively, the coherence factor and the Euclidean distance between the points k_i and k_j. For simplicity, we assume that the coherence factor has the following form (other, more complex forms can also be considered):

$$|\mu(r_{k_ik_j})| = \begin{cases} |\alpha_{r_{k_ik_j}}| \in [0,1) & r_{k_ik_j} \leqslant 1 \\ 0 & \text{otherwise} \end{cases}. \tag{2}$$

If $r_{k_ik_j}>1$, then the cpdf in Eq. (1) becomes independent of i_{k_i}, and we obtain $p_{I_{k_j}|I_{k_i}}(i_{k_j}|i_{k_i})=p_{I_{k_j}}(i_{k_j})=\exp(-i_{k_j}/\mathcal{O}_{k_j})/\mathcal{O}_{k_j}$, which is the familiar (negative) exponential density of the speckle intensity.[18] The correlation in Eq. (2) is assumed to be limited to 1 unit from the center pixel; the implications of this assumption are discussed in detail in Subsection 2.C. This condition can still be met with more general types of correlation (beyond 1 pixel) by preprocessing the data. For example, in the case of an image having a larger correlation, we may apply a spatial-interpolation or downsampling scheme and reduce the correlation to the form given in the above definition.[12,20,21]

Note that the Euclidean distances between the pairs of pixels (i_{k_1},i_{k_2}), (i_{k_2},i_{k_3}), (i_{k_3},i_{k_4}), and (i_{k_4},i_{k_1}) are $\sqrt{2}$ and that the distances between the pairs (i_{k_2},i_{k_4}) and (i_{k_1},i_{k_3}) are 2. In both cases, the distance is greater than 1 unit. By using the coherence factor defined in Eq. (2), we can conclude that these pairs of pixels are conditionally independent given the center pixel i_k. Thus, with the use of Bayes rules, the cpdf of the intensity of the center pixel, i_k, given the four neighbors i_{k_1}, i_{k_2}, i_{k_3}, and i_{k_4}, takes the following form:

$$p_{I_k|I_{k_1},\ldots,I_{k_4}}(i_k|i_{k_1},\ldots,i_{k_4}) = \frac{p_{I_k|I_{k_1}}(i_k|i_{k_1})p_{I_k|I_{k_2}}(i_k|i_{k_2})p_{I_k|I_{k_3}}(i_k|i_{k_3})p_{I_{k|I_{k_4}}}(i_k|i_{k_4})}{[p_{I_k}(i_k)]^3}. \tag{3}$$

Recall that each term in Eq. (3) is precisely known from Eq. (1); therefore, after substitution, we obtain

$$p_{I_k|I_{k_1},\ldots,I_{k_4}}(i_k|i_{k_1},\ldots,i_{k_4}) = \exp\left\{\sum_{j=1}^{4} -\ln[B(i_k,i_{k_j})] - \frac{A(i_k,i_{k_j})}{B(i_k,i_{k_j})} + \ln\left[\mathcal{I}_0\left(\frac{C(i_k,i_{k_j})}{B(i_k,i_{k_j})}\right)\right] - 3\ln[p_{I_k}(i_k)]\right\}, \tag{4}$$

where $A(i_k,i_{k_j})=|\alpha_{r_{kk_j}}|^2 i_{k_j}+i_k$, $B(i_k,i_{k_j})=(1-|\alpha_{r_{kk_j}}|^2)\mathcal{O}_k$, and $C(i_k,i_{k_j})=2(i_k i_{k_j})^{1/2}|\alpha_{r_{kk_j}}|$. In the actual implementation phase of the proposed speckle-reduction algorithm, "$\mathcal{O}_k$,"

which represents the true pixel intensity at index "k," is approximated in Eq. (4) by the empirical average of the observed pixel values over the 3×3 window centered about the kth pixel. Thus the image created through this local averaging is used as an initial estimate of the true intensity.

B. Energy and Potential Functions

Our goal in this subsection is to utilize the cpdf presented in Subsection 2.A to derive the energy and potential functions of the MRF, which fully characterize the MRF. We first observe that the cpdf obtained in Eq. (4) admits the following representation:

$$p_{I_k|I_{k_1},\ldots,I_{k_4}}(i_k|i_{k_1},\ldots,i_{k_4}) = \exp[-U(i_k,i_{k_1},\ldots,i_{k_4})],$$

where

$$U(i_k,i_{k_1},\ldots,i_{k_4}) = V_{C_1}(i_k) + V_{C_2}(i_k,i_{k_1},\ldots,i_{k_4}),$$

$$V_{C_1}(i_k) = 3\ln[p_{I_k}(i_k)],$$

$$V_{C_2}(i_k,i_{k_1},\ldots,i_{k_4}) = \sum_{j=1}^{4}\left\{\frac{A(i_k,i_{k_j})}{B(i_k,i_{k_j})} - \ln\left[\mathcal{I}_0\left(\frac{C(i_k,i_{k_j})}{B(i_k,i_{k_j})}\right)\right] + \ln[B(i_k,i_{k_j})]\right\}. \quad (5)$$

Based on the Hammersley–Clifford theorem,[22,23] it is straightforward to identify the energy function as $U(i_k,i_{k_1},\ldots,i_{k_4})$. Furthermore, by recalling the two types of cliques that were defined in Section 2, we can associate the potential functions $V_{C_1}(i_k)$ and $V_{C_2}(i_k,i_{k_1},\ldots,i_{k_4})$ with the single clique and the pairwise clique, respectively. The above energy function, which is easily shown to be convex by using a convex composition rule,[24,25] will be utilized in the speckle-simulation and speckle-reduction processes.

C. Constraints of the Model on Synthetic Aperture Radar Imagery Data

We will now discuss in depth the implications of the assumption made regarding the coherence factor.

In Subsection 2.A, we assumed that the coherence factor decays to 0 beyond 1 pixel. If we let N denote the sample spacing and R the spatial resolution of the SAR imagery, the aforementioned assumption leads us to the following constraint: $R<2N$. On the other hand, the Nyquist sampling criterion sets another constraint, given by $N\leqslant R$. Therefore the SAR data that will be most suitable for the proposed model must satisfy the following constraint:

$$1\leqslant R/N<2. \quad (6)$$

At this point, the following question comes in mind: How practical is the above constraint? Indeed, numerous existing SAR imaging systems do meet the above criterion, as seen by the following examples, which makes our assumption about the correlation factor realistic from a practical standpoint. The real SAR imageries used in this work, provided by Sandia National Laboratories (SNL),[26] have the ratio $R/N\simeq1.2$. Another SAR system used at SNL, the "Lynx," produces SAR images having a ratio R/N of 1.5 for the earlier system and 1.18 for the most current one.[2,27] Two interferometric SAR systems used by the Brigham Young University Center for Remote Sensing[28] produce SAR imageries with $R/N\simeq1$. In addition, the Japanese Earth Resources Satellite (JERS) SAR system generates SAR images with spatial resolutions of 16 and 14 m along the range and azimuth, respectively; its sample spacing is 12.5 m in both direction, which makes the ratio R/N fall between 1.12 and 1.28.[29] For the European Remote Sensing Satellite (ERS) SAR systems, the ratio R/N is between 1.2 and 2.[30] Finally, the Environment Canada CV-580 airborne SAR produces SAR imageries having the ratio R/N of 1.25 in the range and 1.38 in the azimuth.[31]

3. IMAGE QUALITY ASSESSMENT PARAMETERS

In this paper, four metrics are used to assess the quality of the speckle reduction. The first metric is the mean square error (MSE) between the noise-free (true) I and the denoised images $\hat{I}$, defined by

$$\mathrm{MSE} = K^{-1}\sum_{i=1}^{K}(I_i-\hat{I}_i)^2,$$

where K is the total number of pixels in the image. The second metric is the so-called β parameter,[10,32] introduced by Sattar *et al.*[32] This parameter assesses the quality of edge preservation; it takes values between 0 and 1, where 1 corresponds to the best possible edge preservation. More precisely, the β parameter is defined by

$$\beta = \frac{\Gamma(I_H-\overline{I_H},\widehat{I_H}-\overline{\widehat{I_H}})}{\sqrt{\Gamma(I_H-\overline{I_H},I_H-\overline{I_H})\Gamma(\hat{I_H}-\overline{\widehat{I_H}},\hat{I_H}-\overline{\widehat{I_H}})}},$$

where, for any two images I_1 and I_2, $\Gamma(I_1,I_2)=\Sigma_{i=1}^{K}I_{1_i}I_{2_i}$. The quantities I_H and $\hat{I_H}$ are the high-pass filtered versions (using the Laplacian operator) of I and $\hat{I}$, respectively.

The third metric, the signal-to-mean-square-error ratio[13,33–35] (SMSE) in dB, is defined by

$$\mathrm{SMSE} = 10\log_{10}\left[\frac{\sum_{j=1}^{K}I_j^2}{\sum_{j=1}^{K}(I_i-\hat{I}_i)^2}\right].$$

Finally, the fourth metric is the effective number of looks (ENL), which is often used in practice to estimate the speckle-noise level in SAR imagery.[6,12,13,15,16,35,36] The higher this parameter, the lower the speckle noise. What distinguishes the ENL from the three prior metrics is that it does not require knowledge of the true image, which is typically the case when denoising is applied to real SAR imagery. Thus the ENL is used to assess the speckle-reduction performance in both simulated and real speckled images. The ENL is computed by calculating the mean

and the variance of the intensity over a uniform area:

$$\mathrm{ENL} = \frac{\left(K_0^{-1}\sum_{i\in A}\hat{I}_i\right)^2}{K_0^{-1}\sum_{i\in A}\hat{I}_i^2 - \left(K_0^{-1}\sum_{i\in A}\hat{I}_i\right)^2},$$

where A represents the set of indices corresponding to a uniform area in the image $\hat{I}$ and K_0 is the number of elements in A.

Note that the use of different figures of merit for task-oriented applications (i.e., target detection or pattern recognition) may be more meaningful than employing the above metrics. However, since in this paper we do not address a specific task, considering metrics that assess the noise-reduction properties of the processed imagery, such as those considered in this work, would be appropriate.

4. SIMULATION OF SPECKLED IMAGES

In this section, we utilize the MRF model developed in Section 2 to simulate speckled images with different temperatures from those of true noise-free images. It is to be noted that we are not simulating SAR speckled imagery but rather we are simulating the MRF defined by the Gibbs energy function (5). The proposed simulation approach uses the Metropolis-sampler (MS) algorithm[37] to update the pixel intensity of the image. The simulation of speckled images can be summarized as follows. The first step consists in setting the values of two parameters: the temperature T_0 and the coherence factor $\alpha_{r_{kk_j}}$. The temperature T_0 controls the amount of noise to be introduced into the image, and $\alpha_{r_{kk_j}}$ controls the level of similarity that a pixel has with its four neighbors.

Once the initialization is done, we proceed to update the image pixel intensity: For each pixel intensity i_k of the image, a candidate intensity $i_{k_{\mathrm{new}}}$, other than itself, is randomly chosen. The candidate pixel is accepted with probability $p=\min[1,\exp(-\Delta U/T_0)]$, where $\Delta U = U(i_{k_{\mathrm{new}}},k_{k_1},\ldots,i_{k_4}) - U(i_k,i_{k_1},\ldots,i_{k_4})$ and U is the energy function defined in Eq. (5). This procedure is applied to all pixels of the image, after which the speckled image is returned. A flow chart of the entire simulation algorithm is shown in Fig. 2.

We will now apply this algorithm to an aerial photograph of a scene, which we called the "true scene."[38] Figures 3(b)–3(f) show the results of the simulations for varying initial temperatures T_0. It can be seen that the noise level increases with the temperature, which is accompanied by a decrease in the parameter SMSE, as summarized in Table 1. If the temperature T_0 is set high (e.g., >10), the pixel candidates are all accepted, resulting in a very noisy image [see Fig. 3(f)]. On the other hand, if the temperature is very low (e.g., ≈ 0), most candidate pixels are rejected, resulting in an almost noise-free image, as seen in Fig. 3(b).

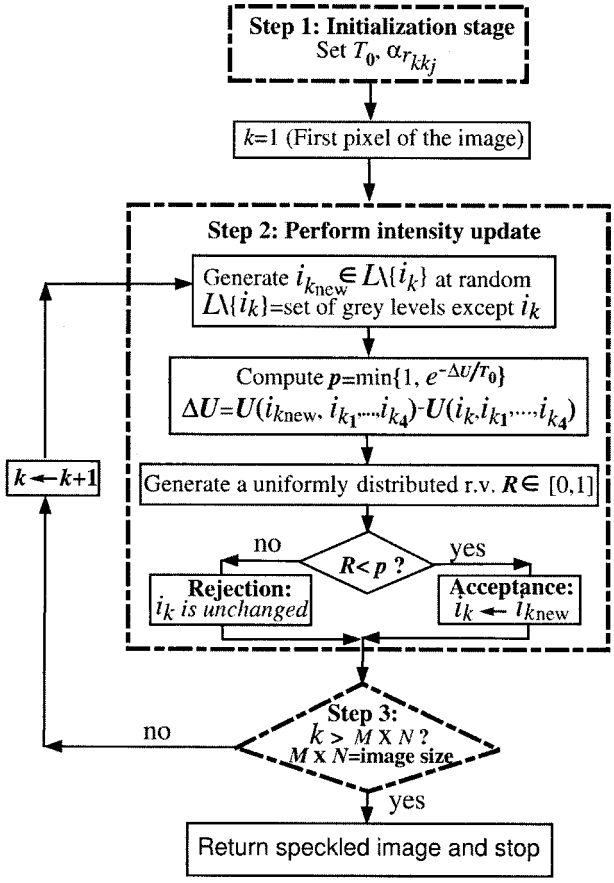

Fig. 2. Flow chart of the SA method undertaken to simulate speckled images.

5. PROPOSED SPECKLE-REDUCTION APPROACH

At the heart of the proposed speckle-reduction technique is a novel pixel-by-pixel nonlinear estimator of the true image. We begin by describing this estimator and exploit the underlying MRF model to provide a simple means for computing it. We also establish the denoising capability of the estimator by showing that the estimated image has a smaller variance than that of the speckled, raw image. We subsequently give a description of the proposed speckle-reduction algorithm that uses the aforementioned nonlinear image estimator.

A. Nonlinear Estimator of the True Image

Given a speckled image I, consider a nonlinear estimator of $\mathcal{O}_k$, the kth pixel of the true image $\mathcal{O}$, defined by the conditional expectation

$$\widehat{\mathcal{O}_k} = \mathsf{E}[I_k | I \setminus \{I_k\}], \tag{7}$$

where $I \setminus \{I_k\}$ is the set of all pixels in the image excluding I_k. Now, using the Markovian nature of I, we can reduce the above estimator to

$$\widehat{\mathcal{O}_k} = \mathsf{E}[I_k | \mathcal{N}_k], \tag{8}$$

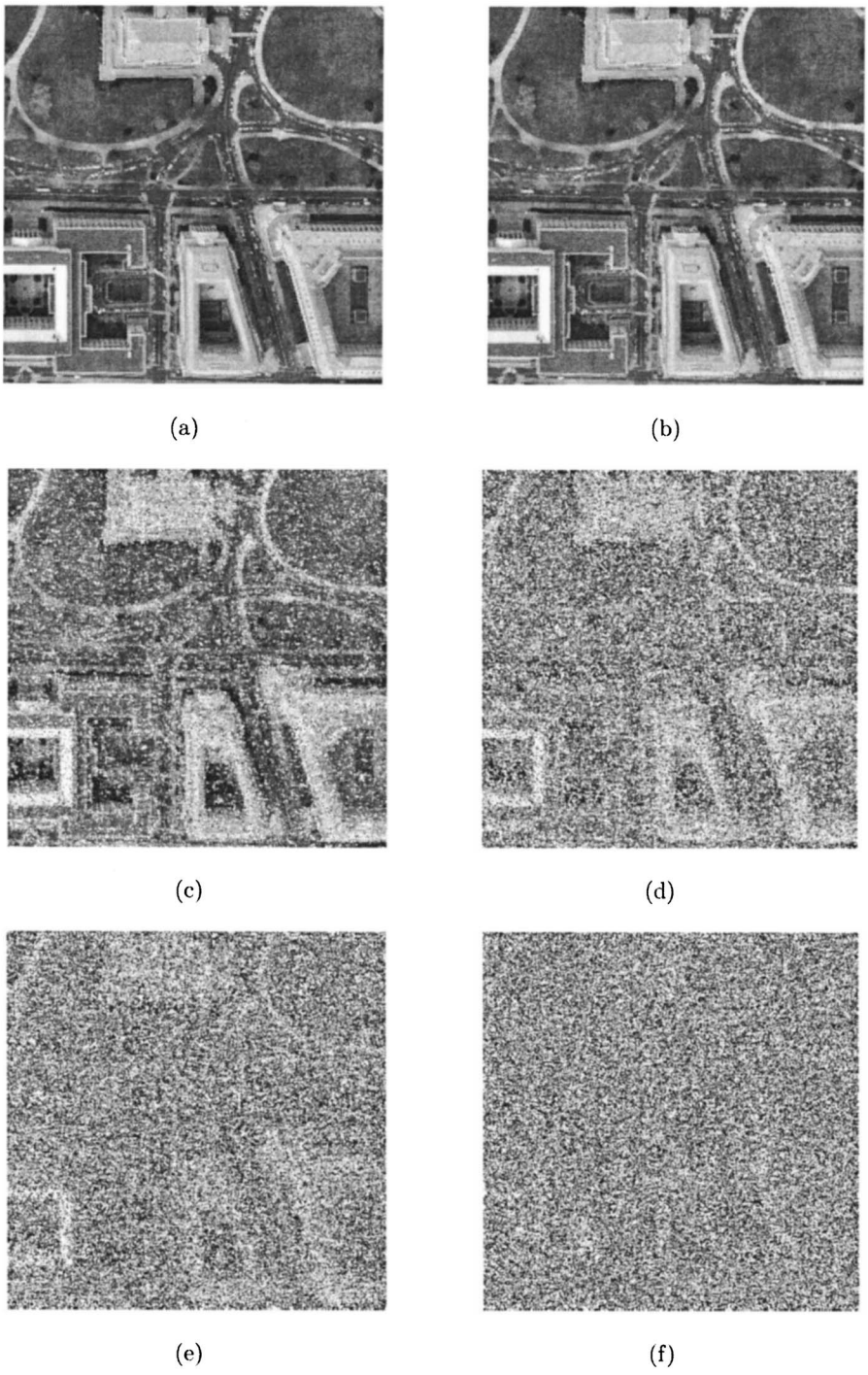

Fig. 3. (a) True scene. (b)–(f) Speckled versions of true scene with (b) $T_0 \to 0$ and SMSE = 27.79 dB, (c) $T_0 = 15$ and SMSE = 12.51 dB, (d) $T_0 = 50$ and SMSE = 8.89 dB, (e) $T_0 = 100$ and SMSE = 7.96 dB, (f) $T_0 = 500$ and SMSE = 7.01 dB.

where $\mathcal{N}_k = \{I_{k_1}, I_{k_2}, I_{k_3}, I_{k_4}\}$ constitutes the set of intensities of the four adjacent pixels of k and the associated cpdf is given in Eq. (4). We next explore some of the properties of $\widehat{\mathcal{O}_k}$. Note that $\mathsf{E}[\widehat{\mathcal{O}_k}] = \mathsf{E}[\mathsf{E}[I_k|\mathcal{N}_k]] = \mathsf{E}[I_k] = \int_0^\infty i p_{I_k}(i) \mathrm{d}i = \int_0^\infty i \mathcal{O}_k^{-1} \exp(-i/\mathcal{O}_k) \mathrm{d}i = \mathcal{O}_k$. Thus $\widehat{\mathcal{O}_k}$ is an unbiased estimator of $\mathcal{O}_k$.

We next show that the variance of $\widehat{\mathcal{O}_k}$ is less than or equal to that of I_k, proving that the unbiased estimated image $\hat{\mathcal{O}}$ is less noisy than the raw image I. Indeed,

Table 1. Variation of the SMSE Parameter as a Function of T_0

T_0	SMSE (dB)
0	29.13
15	12.51
20	11.26
50	8.89
100	7.96
500	7.01

$$\begin{aligned}
&\mathrm{var}[I_k] - \mathrm{var}[\widehat{\mathcal{O}_k}] \\
&\quad = \mathsf{E}[I_k^2] - \mathsf{E}^2[I_k] - (\mathsf{E}[\mathsf{E}^2[I_k|\mathcal{N}_k]] - \mathsf{E}^2[\mathsf{E}[I_k|\mathcal{N}_k]]) \\
&\quad = \mathsf{E}[I_k^2] - \mathsf{E}^2[I_k] - (\mathsf{E}[\mathsf{E}^2[I_k|\mathcal{N}_k]] - \mathsf{E}^2[I_k]) \\
&\quad = \mathsf{E}[I_k^2] - \mathsf{E}[\mathsf{E}^2[I_k|\mathcal{N}_k]] \\
&\quad = \mathsf{E}[\mathsf{E}[I_k^2|\mathcal{N}_k]] - \mathsf{E}[\mathsf{E}^2[I_k|\mathcal{N}_k]] = \mathsf{E}[\mathsf{E}[I_k^2|\mathcal{N}_k] - \mathsf{E}^2[I_k|\mathcal{N}_k]] \\
&\quad \geqslant 0, \qquad (9)
\end{aligned}$$

where the last step follows from Jensen's inequality for conditional expectations.[39] Since $\widehat{\mathcal{O}_k}$ is unbiased, it also follows that $\mathsf{E}[(I-\mathcal{O}_k)^2] \geqslant \mathsf{E}[(\widehat{\mathcal{O}_k}-\mathcal{O}_k)^2]$, which establishes the fact that the proposed estimator has a lower MSE than that in the case when the data are interpreted directly without processing (i.e., if we take I_k as an estimator for $\mathcal{O}_k$).

Finally, the proposed estimate is explicitly given by

$$\begin{aligned}
\widehat{\mathcal{O}_k} &= \int_0^\infty i_k p_{I_k|I_{k_1},\ldots,I_{k_4}}(i_k|i_{k_1},\ldots,i_{k_4})\mathrm{d}i_k \\
&= \int_0^\infty i_k \exp[-U(i_k,i_{k_1},\ldots,i_{k_4})]\mathrm{d}i_k, \qquad (10)
\end{aligned}$$

where $U(i_k,i_{k_1},\ldots,i_{k_4})$ is given by Eq. (5). In practice, the image intensity values are discrete (e.g., in an 8-bit imagery) and the above integral is approximated by a finite sum.

From an intuitive perspective, it is reasonable to exclude the pixel intensity I_k from the conditional estimation of the noisy pixel intensity I_k at point k given its neighbors. Indeed, in the proposed algorithm for speckle reduction (which will be described in Subsection 5.B), a detection mechanism is placed to leave untouched the "less noisy" pixel based on the threshold set by the parameters δ and γ and process only the ones that have failed the threshold test (called the "uniformity test" in Subsection 5.B) therefore the pixel I_k at point k is regarded as suspicious and unreliable, and it is discarded in the estimation of the true pixel intensity $\mathcal{O}_k$.

B. Description of the Proposed Speckle-Reduction Algorithm

A simulated annealing (SA) approach of speckle reduction using the proposed MRF model was investigated earlier[15,16] and was shown to yield good results compared with a well-known speckle-reduction algorithm.[6] However, a large number of iterations (i.e., 80 iterations[16]) is needed to denoise the speckled SAR imagery. Therefore, even though the despeckled image obtained is impressive, the major drawback of the SA-based algorithm is its computational complexity. This issue is resolved in this paper thanks to the nonlinear estimation approach described in Subsection 5.A. The narrative description of the algorithm will be provided first, followed by its detailed mathematical description.

The proposed despeckling algorithm is implemented as follows. After the initialization of the algorithm's parameters, the image is scanned and the "uniformity test" is performed on every pixel. The first purpose of the uniformity test is to detect the "noisy" pixels based on a threshold that is set by the user. The second purpose is to differentiate a line (e.g., a road) from noisy pixels; edges of lines can be confused with spatial noise due to the large variability in intensity. This uniformity test and its control parameters allow us to handle the trade-off between reducing speckle noise and oversmoothing. Proper selection of the control parameters allows us to reduce noise while maintaining the high spatial content in the true scene. The test consists in computing the intensity variability within a window W_k (of size 3×3 here) centered about the pixel k. This step is described in detail in the mathematical description below. Low variability in intensity within the window W_k or along a direction (in the presence of lines) is a sign of a relative intensity homogeneity, which means that the pixel in question is "less noisy" based on the threshold set by the parameters δ and γ. In this case, the pixel is left untouched. However, if the variability in intensity is high, it is a sign of the presence of noise. The pixel is therefore replaced with the estimate given in Eq. (10). Based on our experience, we have observed that restricting the set of possible values of i_k in Eq. (10) from the set $\{0,\ldots,255\}$ to the set of intensity values corresponding to pixels in the window $W_k = \{W_{k_0},\ldots,W_{k_8}\}$ does not alter the results significantly. Indeed, the probability of any pixel intensity outside the window W_k being nearly 0, their contribution to the estimated intensity value is negligible. In addition, this approximation has the advantage of being faster.

The detailed mathematical description of the algorithm is given below:

1. Step 1: Initialization Stage of the Algorithm

The following parameters are chosen on a case-by-case basis:

- The coherence factor $\alpha_{r_{kk_j}}$.
- The parameter δ, which is the threshold for line or noise detection.
- The parameter γ, which is the threshold number of pixels within the window W_k of size 3×3 centered in i_k whose variations are below δ.

2. Step 2: Performing the Uniformity Test

Let us consider the kth pixel with intensity i_k. The window W_k is extracted, and intensity variations are computed about the center pixel i_k as follows: $\Delta W_{kk_j} = |i_k - W_{k_j}|$, $j=1,\ldots,8$. Next, evaluate the following [see Figs. 4(b) and 4(c)]:

1. $N_k = \Sigma_{j=1}^{8}(\Delta W_{kk_j} < \delta)$. This is the number of pixels within W_k whose intensities are similar (i.e., less than δ apart) to the intensity of the center pixel.
2. Perform the uniform-neighborhood test: $U = (N_k \geqslant \gamma)$.
3. Horizontal line test: $H = \{(\Delta W_{kk_1} < \delta)$ and $(\Delta W_{kk_5} < \delta)\}$.
4. Vertical line test: $V = \{(\Delta W_{kk_3} < \delta)$ and $(\Delta W_{kk_7} < \delta)\}$.
5. First oblique line test: $O_1 = \{(\Delta W_{kk_2} < \delta)$ and $(\Delta W_{kk_6} < \delta)\}$.
6. Second oblique line test: $O_2 = \{(\Delta W_{kk_4} < \delta)$ and $(\Delta W_{kk_8} < \delta)\}$.

Line/noise detection test:

Test: Is (U or H or V or O_1 or O_2) true? If yes, the intensity i_k is unchanged. If no, a large variability has been detected and i_k is possibly noisy. Therefore the algorithm proceeds to update the intensity.

3. Step 3: Performing the Intensity Update

1. Compute $p_{I_k|I_{k_1},\ldots,I_{k_4}}(i_k|i_{k_1},\ldots,i_{k_4})=\exp[-U(i_k, i_{k_1},\ldots,i_{k_4})]$, where $i_k=W_{k_j}, j=0,\ldots,8$.
2. Intensity update: $i_k \leftarrow \widehat{\mathcal{O}_k}$, where

$$\widehat{\mathcal{O}_k}=\sum_{i_k=W_{k_0}}^{W_{k_8}} i_k p_{I_k|I_{k_1},\ldots,I_{k_4}}(i_k|i_{k_1},\ldots,i_{k_4}).$$

4. Step 4: Repeat Steps 2 and 3 for the Next Pixel

Increment k and go to step 2 until $k=M\times N$, $M\times N$ being the size of the image. The flow chart given in Fig. 4(a) summarizes the proposed speckle-reduction algorithm.

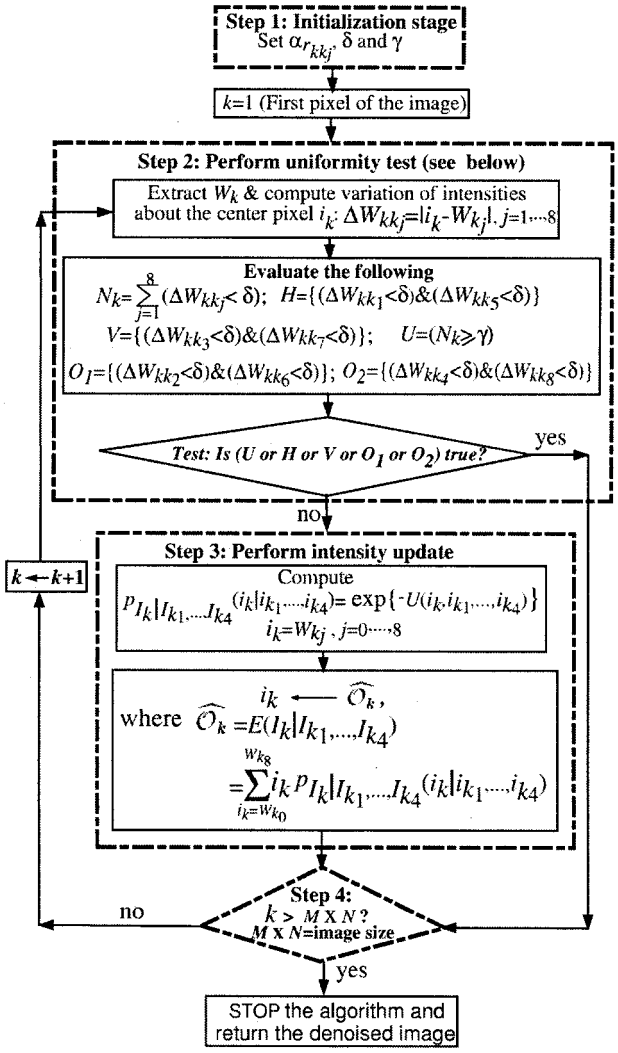

(a)

W_{k_2}	W_{k_3}	W_{k_4}
W_{k_1}	W_{k_0}	W_{k_5}
W_{k_8}	W_{k_7}	W_{k_6}

(b)

ΔW_{kk_2}	ΔW_{kk_3}	ΔW_{kk_4}
ΔW_{kk_1}	0	ΔW_{kk_5}
ΔW_{kk_8}	ΔW_{kk_7}	ΔW_{kk_6}

(c)

Fig. 4. (a) Flow chart of the proposed speckle-reduction approach, (b) window W_k centered on the kth pixel, (c) corresponding window after subtraction of i_k.

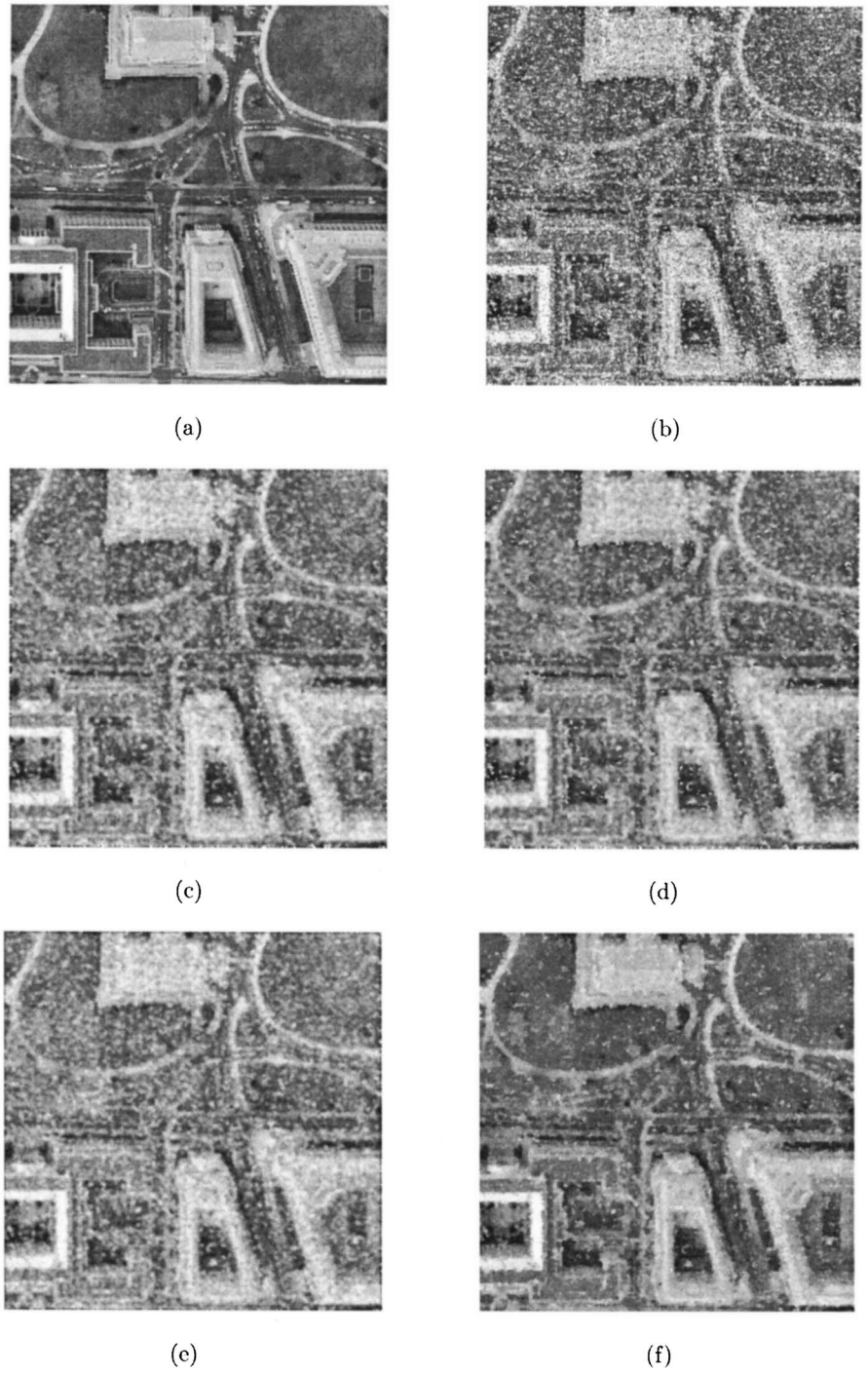

Fig. 5. (a) True scene, (b) speckled version of true scene with $T_0=15$ and SMSE=12.51 dB, (c) modified Lee filtered version, (d) Gamma filtered version, (e) enhanced Frost filtered version, (f) proposed approach.

6. EXPERIMENTAL RESULTS AND ANALYSIS

A. Speckle Reduction of Simulated Speckled Image

The speckle-reduction approach described in Subsection 5.B is applied here to the simulated speckled image obtained in Fig. 3(c). Well-known speckle removal filters such as the Gamma MAP, the modified Lee, and the enhanced Frost filters[6] are compared against our proposed approach. The speckle removal results are shown in Figs. 5(c)–5(f). The metrics ENL, MSE, β, and SMSE defined in

Table 2. Results of Speckle Reduction Using the Simulated Speckled Image

Technique	ENL	MSE	β	SMSE (dB)
Noisy image	17.39	1164.6	0.2291	12.51
Gamma filtered	61.39	476.78	0.3355	16.39
Modified Lee filtered	71.16	433.76	0.3885	16.80
Enhanced Frost filtered	71.15	431.56	0.3390	16.82
Proposed approach	85.73	246.95	0.4796	19.24

Section 3 are measured and reported in Table 2. The visual comparison as well as the numerical results allows us to claim that the proposed approach performs better. In particular, in addition to the good speckle reduction, the resulting images are not blurred and the features are better preserved.

As expected, the proposed speckle-reduction approach applied on the simulated images performs better compared with the standard methods (various images with different amounts of noise, not shown here, have been tested and present the same trend). This should not come as a surprise, since the Gibbs energy function (5) was used to simulate the speckled image and also in the despeckling process. These results were shown here as a way to confirm the validity of the proposed speckle-reduction algorithm on simulated data. The unequivocal

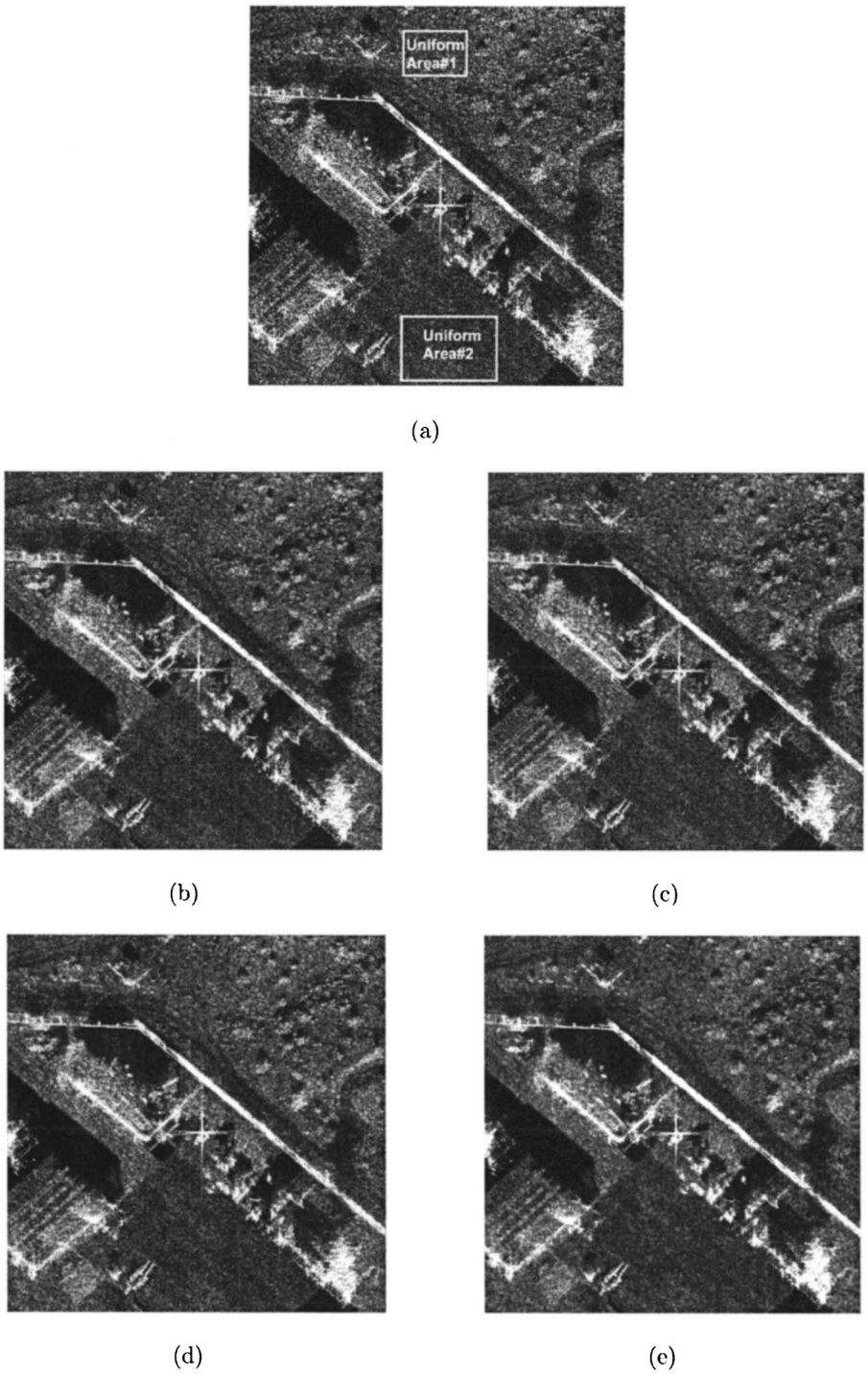

Fig. 6. (a) Image 1. (b)–(e) Processed images using (b) modified Lee, (c) Gamma MAP, (d) enhanced Frost, and (e) proposed approaches.

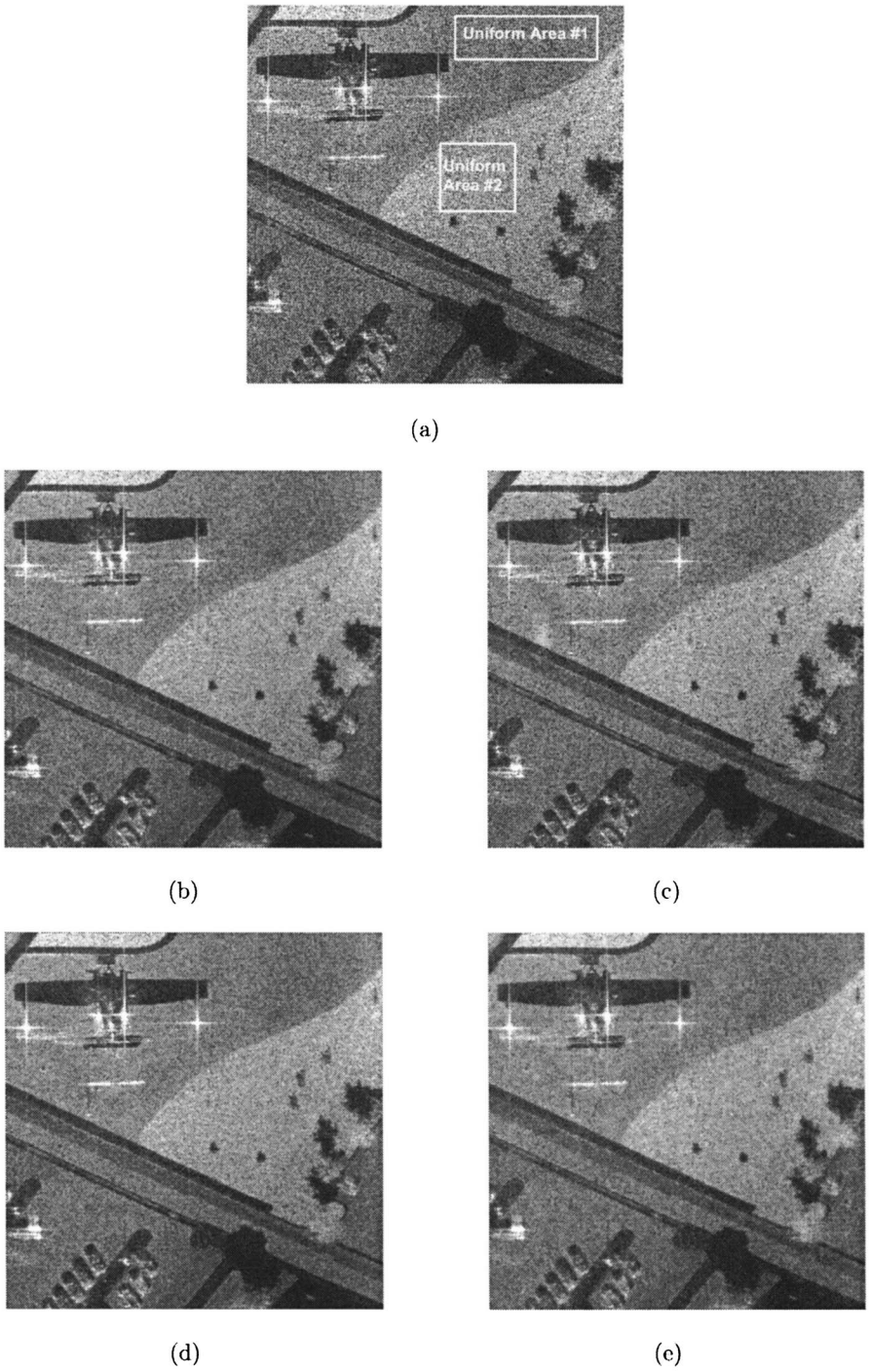

Fig. 7. (a) Image 2. (b)–(e) Processed images using (b) modified Lee, (c) Gamma MAP, (d) enhanced Frost, and (e) proposed approaches.

proof of superiority of the proposed approach will be illustrated on real SAR images and is discussed in Subsection 6.B.

B. Speckle Reduction Using Real Synthetic Aperture Radar Images

In this subsection, various speckle-reduction filters, such as the Lee,[5] the Frost,[9] the Kuan,[8] the modified Lee, the enhanced Frost, and the Gamma MAP filters,[6] have been tested on real SAR images. The best results obtained by using the modified Lee, the Gamma MAP, and the enhanced Frost are compared against the proposed speckle-reduction approach. Two real SAR images[26] are used for this purpose.

The first image, shown in Fig. 6(a), is called image 1, and it is of size 700×700. The second image, of size 600×600, is shown in Fig. 7(a); this will be called image 2. The two uniform areas shown in these images are used to monitor the speckle reduction via the ENL metric. This metric will be the only one used to assess the noise filtering quality for real SAR images, since the other metrics require knowledge of the true image. At this stage of the

work, the parameters of the algorithm are set manually on a case-by-case basis. the parameters used are $\alpha_{r_{kk_i}}=0.90$, $\delta=5$, and $\gamma=4$ for image 1 and $\alpha_{r_{kk_j}}=0.93$, $\delta=2$, and $\gamma=4$ for image 2.

The speckle-reduction process for image 1 is presented in Figs. 6(b)–6(e), and the numerical results are summarized in Table 3. The proposed approach gives ENL =8.57 and ENL=14.17 against ENL=8.08 and ENL =13.24 for the enhanced Frost. For the two areas tested, the ENL is higher for the proposed approach than for the other filters. The same trend is observed with image 2 as seen in Figs. 7(b)–7(e) and Table 4, where the proposed approach produces ENL=46.65 and ENL=99.14 against ENL=44.34 and ENL=88.39 for the enhanced Frost.

Table 3. Speckle Reduction Using Image 1[a]

Technique	ENL (Area 1)	ENL (Area 2)
Image 1 (noisy)	2.66	3.33
Gamma filtered version	7.64	12.51
Modified Lee filtered version	7.96	13.07
Enhanced Frost filtered version	8.08	13.24
Proposed approach	8.57	14.17

[a]The higher ENL is, the better is the speckle reduction.

Table 4. Speckle Reduction Using Image 2[a]

Technique	ENL (Area 1)	ENL (Area 2)
Image 2 (noisy)	10.83	12.19
Gamma filtered version	35.46	59.94
Modified Lee filtered version	43.14	86.09
Enhanced Frost filtered version	44.34	88.39
Proposed approach	46.65	99.14

[a]The higher ENL is, the better is the speckle reduction.

Generally, lack of features preservation and blur (or oversmoothing) are some of the common adverse effects that a filter may have on an image in the speckle denoising process. We will therefore analyze the effects of the various filters on image 1. In Fig. 6(a), one can see the bright "cross" that will be used to assess the image degradation of each filter. The zoomed versions of the cross area before and after speckle reduction using the various filters are presented in Fig. 8. It is clear to us that our despeckled image, which is shown in Fig. 8(e), preserves the edges better than the standard denoising methods. For example, the true width of the cross is maintained when our method is used [see Fig. 8(e)], while the use of standard methods (filters) tends to shrink the width [see Figs. 8(b)–8(d)]. Additionally, certain seemingly false isolated dark pixels that appear on the noisy cross [see Fig. 8(a)] have been smeared by the standard methods. In contrast, the proposed approach has apparently identified these pixels as noisy pixels and effectively eliminated their erroneous effect. After the filtering process, only the proposed approach [see Fig. 8(e)] has extracted the noisy pixels from the scene without blurring the image. Another demonstration of the superiority of our filtering technique can be found in Fig. 9. It represents an approximate profile of the point-spread function before and after speckle reduction, which is extracted from Fig. 8(a). This experimental estimate of the "line response" of each filter is often used in practice by SAR-imagery specialists to assess the resolution degradation brought about by the denois-

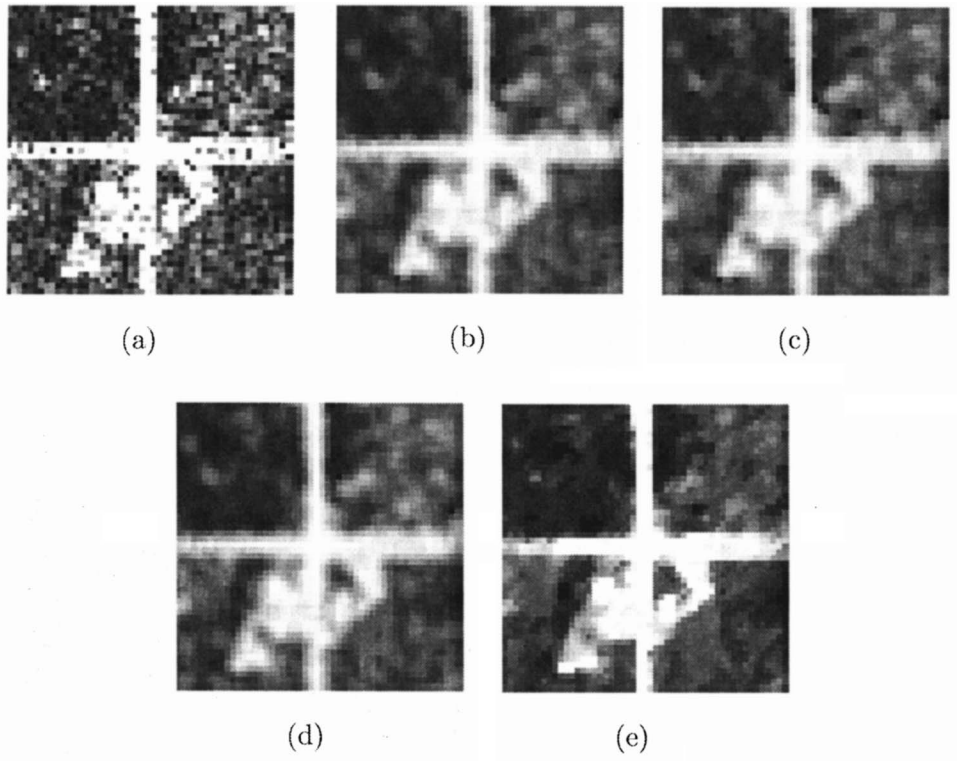

Fig. 8. (a) Zooming around the "cross" of image 1. (b)–(e) Processed images using (b) modified Lee, (c) Gamma MAP, (d) enhanced Frost, and (e) proposed approaches.

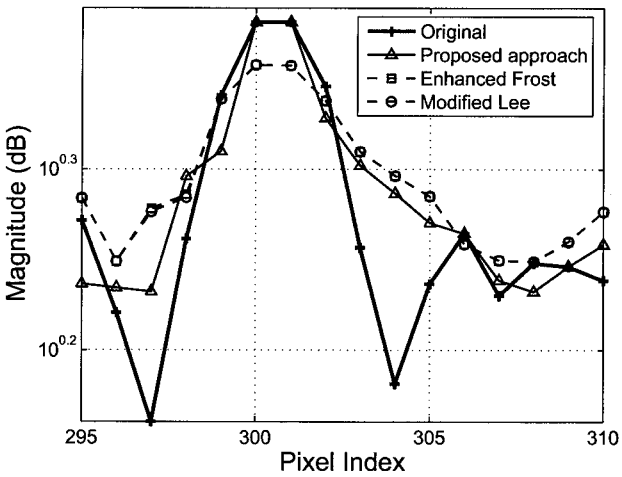

Fig. 9. Image 1: point-spread-function-like curve before (+) and after filtering using the proposed (△), enhanced Frost (□), and modified Lee (○) approaches.

ing process. An inspection of Fig. 9 reveals that the proposed approach produces a narrow line response compared with that of other methods. The curve (or line response) corresponding to the proposed approach has preserved its initial peak, which means that the initial noise-free bright area has not been blurred. The enhanced Frost and modified Lee outputs in that figure have lost their initial peak.

7. CONCLUSION

We introduced a novel convex Gibbs energy function for speckled SAR imagery in the context of a MRF. The model is developed in accord with the physical, spatial statistical properties of speckle. This Gibbs energy function is used in conjunction with the MS algorithm to generate simulated speckled images. Speckle reduction is then obtained through a novel nonlinear estimator, based on a conditional expectation, which utilized the derived Gibbs energy function. A comparative analysis of our results against common speckle-reduction techniques such as the Gamma MAP, the modified Lee, and the enhanced Frost illustrates the superiority of the proposed approach. The success of our filtering approach is attributed to the capability of the derived Gibbs energy function, within the MRF model, to capture the intrinsic properties of speckle in SAR imagery.

ACKNOWLEDGMENTS

The authors thank Armin Doerry at Sandia National Laboratories for valuable discussions and providing the SAR imagery used in this work. We also thank David G. Long, Director of the Center for Remote Sensing, Brigham Young University, for his valuable comments during the preparation of this manuscript.

Ousseini Lankoande can be reached by e-mail at lankoande@ece.unm.edu. His mailing address is Department of Electrical and Computer Engineering, MSC01 1100, 1 University of New Mexico, Albuquerque, New Mexico 87131-0001.

REFERENCES

1. G. Franceschetti and R. Lanari, *Synthetic Aperture Radar Processing* (CRC Press, 1999).
2. A. Doerry and F. Dickey, "Synthetic aperture radar," Opt. Photon. News, November 2004, pp. 28–33.
3. F. T. Ulaby, R. K. Moore, and A. K. Fung, *Radar Remote Sensing and Surface Scattering and Emission Theory*, Vol. 2 of Microwave Remote Sensing: Active and Passive (Addison-Wesley, 1982).
4. F. Ulaby, F. Kouyate, B. Brisco, and T. Williams, "Texture information in SAR images," IEEE Trans. Geosci. Remote Sens. **24**, 235–245 (1986).
5. J. Lee, "Speckle analysis and smoothing of synthetic aperture radar images," Comput. Graph. Image Process. **17**, 24–32 (1981).
6. A. Lopes, R. Touzi, and E. Nezry, "Adaptive speckle filters and scene heterogeneity," IEEE Trans. Geosci. Remote Sens. **28**, 992–1000 (1990).
7. T. R. Crimmins, "Geometric filter for speckle reduction," Appl. Opt. **24**, 1438–1443 (1985).
8. D. T. Kuan, A. A. Sawchuk, T. C. Strand, and P. Chavel, "Adaptive noise smoothing filter for images with signal-dependent noise," IEEE Trans. Pattern Anal. Mach. Intell. **TPAMI-7**, 165–177 (1985).
9. V. Frost, J. Stiles, K. Shanmugan, and J. Holtzman, "A model for radar images and its application to adaptive digital filtering of multiplicative noise," IEEE Trans. Pattern Anal. Mach. Intell. **PAMI-4**, 157–165 (1982).
10. A. Achim, P. Tsakalides, and A. Bezerianos, "SAR image denoising via Bayesian wavelet shrinkage based on heavy tailed modeling," IEEE Trans. Geosci. Remote Sens. **41**, 1773–1784 (2003).
11. F. Argenti and L. Alparone, "Speckle removal from SAR images in the undecimated wavelet domain," IEEE Trans. Geosci. Remote Sens. **40**, 2363–2374 (2002).
12. C. Oliver and S. Quegan, *Understanding Synthetic Aperture Radar Images* (SciTech, 2004).
13. H. Xie, L. Pierce, and F. Ulaby, "SAR speckle reduction using wavelet denoising and Markov random field modeling," IEEE Trans. Geosci. Remote Sens. **40**, 2196–2212 (2002).
14. R. Touzi, "A review of speckle filtering in the context of estimation theory," IEEE Trans. Geosci. Remote Sens. **40**, 2392–2404 (2002).
15. O. Lankoande, M. M. Hayat, and B. Santhanam, "Speckle reduction of SAR images using a physically based Markov random field model and simulated annealing," in *Algorithms for Synthetic Aperture Radar Imagery XII*, F. G. Zelnio and F. D. Garber, eds., Proc. SPIE **5808**, 210–221 (2005).
16. O. Lankoande, M. M. Hayat, and B. Santhanam, "Speckle modeling and reduction in synthetic aperture radar imagery," in *Proceedings of the IEEE International Conference on Image Processing* (IEEE, 2005), Vol. 3, pp. 317–320.
17. O. Lankoande, M. M. Hayat, and B. Santhanam, "Segmentation of SAR images based on Markov random field model," in *Proceedings of the IEEE International Conference on Systems, Man and Cybernetics* (IEEE, 2005), pp. 2956–2961.
18. J. Dainty, *Topics in Applied Physics: Laser Speckle and Related Phenomena* (Springer-Verlag, 1984).
19. J. Goodman, *Statistical Optics* (Wiley-Interscience, 1985).
20. R. Keys, "Cubic convolution interpolation for digital image processing," IEEE Trans. Acoust. Speech Signal Process. **ASSP-29**, 1153–1160 (1981).
21. S. Quegan, "Interpolation and sampling in SAR images," IEEE Trans. Geosci. Remote Sens. **28**, 641–646 (1990).
22. J. Besag, "Spatial interaction and the statistical analysis of lattice systems," J. R. Stat. Soc. Ser. B. Methodol. **6**, 192–236 (1974).
23. R. Kinderman and J. Snell, *Markov Random Fields and Their Applications* (American Mathematical Society, 1980).
24. M. Tawarmalani and N. V. Sahinidis, "A polyhedral branch-

and-cut approach to global optimization," Math. Program. **103**, 225–249 (2005).
25. C. Maheshwari, A. Neumaier, and H. Schichl, "Convexity and concavity detection," Tech. Rep., Universitat Wien, A-1010 Vienna, Austria (July 2003), http://www.mat.univie.ac.at/~herman/papers.html.
26. Courtesy of Armin Doerry at Sandia National Laboratories, awdoerr@sandia.gov (personal communication, October 25, 2004).
27. S. Tsunoda, F. Pace, J. Stence, M. Woodring, W. H. Hensley, A. Doerry, and B. Walker, "Lynx: a high-resolution synthetic aperture radar," in *Radar Sensor Technology IV*, R. Trebits and J. L. Kurtz, eds., Proc. SPIE **3704**, 20–27 (1999).
28. Courtesy of David G. Long, Brigham Young University, Director of the Center for Remote Sensing, 459 Clyde Building, Provo, Utah 84602, http://www.cers.byu.edu/ (personal communication, October 20, 2005).
29. Australian Government, "JERS SAR processing levels" (November 2005), http://www.ga.gov.au/acres/prod_ser/jers_lev.htm.
30. Australian Government, "ERS SAR Processing Levels" (November 2005), http://www.ga.gov.au/acres/prod_ser/ers_levs.htm.
31. B. Scheuchl, D. Flett, G. Staples, G. Davidson, and I. Cumming, "Preliminary classification results of simulated RADARSAT-2 polarimetric sea ice data," presented at the Workshop on Applications of SAR Polarimetry and Polarimetric Interferometry, ESA/ESRIN, Frascati, Italy (January 14–16, 2003).
32. F. Sattar, L. Floreby, G. Salomonsson, and B. Lovstrom, "Image enhancement based on a nonlinear multiscale method," IEEE Trans. Image Process. **6**, 888–895 (1997).
33. A. Achim, A. Bezerianos, and P. Tsakalides, "Wavelet-based ultrasound image denoising using an alpha-stable prior probability model," in *Proceedings of the IEEE International Conference on Image Processing* (IEEE, 2001), Vol. 2, pp. 221–224.
34. S. Gupta, R. C. Chauhan, and S. C. Sexana, "Wavelet-based statistical approach for speckle reduction in medical ultrasound images," Med. Biol. Eng. Comput. **42**, 189–192 (2004).
35. L. Gagnon and A. Jouan, "Speckle filtering of SAR images—a comparative study between complex-wavelet-based and standard filters," in *Wavelet Applications in Signal and Image Processing V*, A. Aldroubi, A. F. Laine, and M. A. Unser, eds., Proc. SPIE **3169**, 80–91 (1997).
36. J. R. Sveinsson and J. A. Benediktsson, "Almost translation invariant wavelet transformations for speckle reduction of SAR images," IEEE Trans. Geosci. Remote Sens. **41**, 2404–2408 (2003).
37. N. Metropolis, A. Rosenbluth, M. Rosenbluth, A. Teller, and E. Teller, "Equations of state calculations by fast computing machines," J. Chem. Phys. **21**, 1087–1092 (1953).
38. Carnegie Mellon University, Vision and Autonomous Systems Center's Image Database, "Parks and Roads," (Nov. 2005), http://vasci.ri.cmu.edu//idb/html/stereo/houseof/index.html.
39. Y. S. Chow and H. Teicher, *Probability Theory* (Springer-Verlag, 1997).